Mechanical properties and failure modes of additively-manufactured chiral metamaterials based on Euclidean tessellations: an experimental and finite element study

Luke Mizzi, Arrigo Simonetti and Andrea Spaggiari
Department of Engineering Sciences and Methods (DISMI), University of Modena and Reggio Emilia, Reggio Emilia, Italy

Abstract

Purpose – The "chiralisation" of Euclidean polygonal tessellations is a novel, recent method which has been used to design new auxetic metamaterials with complex topologies and improved geometric versatility over traditional chiral honeycombs. This paper aims to design and manufacture chiral honeycombs representative of four distinct classes of 2D Euclidean tessellations with hexagonal rotational symmetry using fused-deposition additive manufacturing and experimentally analysed the mechanical properties and failure modes of these metamaterials.

Design/methodology/approach – Finite Element simulations were also used to study the high-strain compressive performance of these systems under both periodic boundary conditions and realistic, finite conditions. Experimental uniaxial compressive loading tests were applied to additively manufactured prototypes and digital image correlation was used to measure the Poisson's ratio and analyse the deformation behaviour of these systems.

Findings – The results obtained demonstrate that these systems have the ability to exhibit a wide range of Poisson's ratios (positive, quasi-zero and negative values) and stiffnesses as well as unusual failure modes characterised by a sequential layer-by-layer collapse of specific, non-adjacent ligaments. These findings provide useful insights on the mechanical properties and deformation behaviours of this new class of metamaterials and indicate that these chiral honeycombs could potentially possess anomalous characteristics which are not commonly found in traditional chiral metamaterials based on regular monohedral tilings.

Originality/value – To the best of the authors' knowledge, the authors have analysed for the first time the high strain behaviour and failure modes of chiral metamaterials based on Euclidean multi-polygonal tessellations.

Keywords Auxetic metamaterials, Chiral honeycombs, Additive manufacturing, 2D Euclidean tessellations

Paper type Research paper

1. Introduction

Auxetic metamaterials are structured-materials which possess a negative Poisson's ratio (Evans *et al.*, 1991; Bertoldi *et al.*, 2017; Ren *et al.*, 2018). This unusual property is derived from the geometry of the system and is known to be scale-independent. This means that the geometries and deformation mechanisms which give rise to auxeticity can be reproduced at various levels ranging from additively-manufactured macroscale systems, to microscale architectures and, even, as small as nanoscale crystal lattices. Auxetic materials are also characterised by a number of additional unusual and advantageous properties which are directly derived from their negative Poisson's ratio, including large indentation resistance and energy absorption properties (Scarpa *et al.*, 2006; Duncan *et al.*, 2018; Linforth *et al.*, 2021), the ability to undergo synclastic curvature (Wang and Hu, 2014; Papadopoulou *et al.*, 2017; Jang *et al.*, 2022) and superior acoustic and photonic properties (Valente *et al.*, 2016; Zheludev and Plum, 2016; Dudek *et al.*, 2022, 2023) with respect to conventional materials. These properties can also be combined with other related geometrically-tailored characteristics such adjustable stiffness and void/pore volume fraction. This makes auxetic metamaterials extremely well-suited for applications which require the use of highly porous lightweight materials such as biomedical scaffolds (Park and Kim, 2013; Chow *et al.*, 2022) and morphing wing airfoils (Spadoni and Ruzzene, 2007; Airoldi *et al.*, 2015) and/or materials capable of undergoing large deformations such as flexible robotic joints (Kaur and Kim, 2019; Lee *et al.*, 2021), deployable aerospace components (Hassan *et al.*, 2008; Jacobs *et al.*, 2012) and perforated skin-grafts (Mizzi, *et al.*, 2015).

The current issue and full text archive of this journal is available on Emerald Insight at: **https://www.emerald.com/insight/1355-2546.htm**

Rapid Prototyping Journal
30/11 (2024) 59–71
Emerald Publishing Limited [ISSN 1355-2546]
[DOI 10.1108/RPJ-06-2023-0190]

Received 8 June 2023
Revised 29 September 2023
23 January 2024
Accepted 1 February 2024

There are a variety of geometries and deformation mechanisms which give rise to auxetic behaviour. The majority of these structures can be broadly classified into four main categories: re-entrant geometries (Masters and Evans, 1996; Wan *et al.*, 2004; Zied *et al.*, 2015), rotating rigid unit modes (Grima and Evans 2000, 2006; Grima *et al.*, 2005; Strek *et al.*, 2015; Mizzi *et al.*, 2020a), origami/folding systems (Schenk and Guest, 2013; Silverberg *et al.*, 2014) and chiral honeycombs (Wojciechowski, 1989; Spadoni *et al.*, 2009; Alderson *et al.*, 2010; Shim *et al.*, 2013; Wu *et al.*, 2019; Bacigalupo and Gambarotta, 2020). The latter class of metamaterials is of particular interest for the purposes of this study. Chiral honeycombs are a group of metamaterials which are characterised by "chirality" or "handedness". This means that these systems possess sub-units which possess no axis of mirror-symmetry and, in typical chiral honeycombs, this property extends to the entire representative volume element or repeating unit-cell which defines the metamaterial structure. The first chiral system proposed in literature was the hexachiral honeycomb (Prall and Lakes, 1997) [see Figure 1(a)]; an axi-asymmetric system possessing rotational symmetry of order 6, which is characterised by a circular node connected to six adjacent congruent nodes through tangentially-attached ligaments and deforms by rotation of the nodes and flexure of ligaments. The design of this system was followed by the development of analogous systems with quadratic and trigonal rotational symmetry, namely tetrachiral (Alderson *et al.*, 2010; Bacigalupo and Gambarotta, 2014; Mizzi *et al.*, 2018a, 2018b; Zhong *et al.*, 2019) and trichiral (Alderson *et al.*, 2010; Shiyin, Xiuchang and Hongxing, 2015; Mizzi *et al.*, 2018a, 2018b) honeycombs [see Figure 1(b) and (c)], along with hierarchical (Mousanezhad *et al.*, 2016; Zhu *et al.*, 2019; Mizzi and Spaggiari, 2020) [Figure 1(e) and (d)] and irregular (Mizzi *et al.*, 2018a, 2018b) [Figure 1(f)] variants of these systems. Furthermore, subclasses of related structures known as anti-chiral (Sigmund *et al.*, 1998; Alderson *et al.*, 2010; Chen *et al.*, 2013; Bacigalupo and De Bellis, 2015; Hu *et al.*, 2019) and meta-chiral honeycombs (Grima *et al.*, 2008), which exhibit chirality at a sub-unit level only (i.e. individual node and ligament connections) while possessing at least one global of axis of mirror-symmetry and possess the ability to exhibit auxetic behaviour, have also been proposed.

Figure 1 (a) Hexachiral honeycomb, (b) tetrachiral honeycomb, (c) trichiral honeycomb, (d) fractal hexachiral system (Zhu *et al.*, 2019), (e) truss-based hierarchical hexachiral honeycomb (Mizzi and Spaggiari, 2020) and (f) an irregular hexachiral honeycomb (Mizzi *et al.*, 2018a, 2018b) with rotational symmetry of order 2

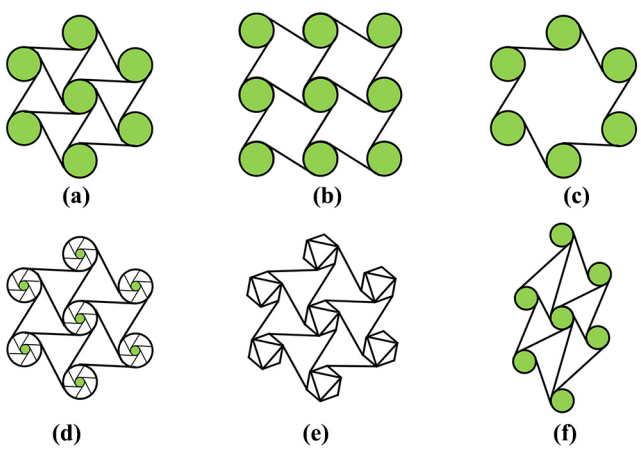

Source: Authors' own work

The chiral honeycombs shown in Figure 1 can all be tessellated periodically in 2D space based on monohedral tilings. The tetrachiral and trichiral honeycombs can be represented by square and hexagon tilings, respectively, while the hexachiral honeycombs can be represented by a triangular tiling; an equilateral triangle in the case of the regular, fractal and hierarchical hexachiral shown in Figure 1(a), (d) and (e), and scalene triangles in the case of the irregular chiral system [Figure 1(f)]. However, besides these chiral honeycombs, other chiral systems based on polyhedral tessellations and their dual counterparts also exist. These chiral honeycombs, which are formed through "chiralisation" (Mizzi and Spaggiari 2021, 2022; Mizzi *et al.*, 2023) of 2D Euclidean tessellations, have also been shown to have the capability of exhibiting auxetic behaviour as well as a considerable range of versatility in terms of possible Poisson's ratios and Young's moduli which may be obtained through tailoring of the metamaterial geometry. This versatility, which by far exceeds that of traditional chiral honeycombs based on regular monohedral hexagonal, square and triangular tilings, arises from the additional geometric complexity of the base tessellation and it has been shown, in previous works (Mizzi and Spaggiari 2021, 2022; Mizzi *et al.*, 2023), that the large spectrum of mechanical properties may be obtained without the loss of the global rotational symmetry of the overall system.

Thus far, the mechanical properties and deformation behaviours of these novel chiral metamaterials have been primarily investigated through the use of finite element (FE) simulations under linear geometric loading using periodic boundary conditions. In this work, we aim to obtain a more comprehensive understanding of these systems by investigating their deformation behaviour and mechanical properties under high-strain compressive loading up to failure through the use experimental tests on additively-manufactured prototypes as well as FE simulations under nonlinear geometric conditions. The failure modes of these chiral metamaterials were also observed and analysed for the first time, providing useful insights on the fracture propagation patterns and energy absorption potential of these structures. This information is necessary for the implementation of these systems in impact resistance applications and dynamic loading conditions as well as for future design of other monohedral and polyhedral tessellation-based chiral metamaterials with similar topologies.

2. Methodology

In this section, the design and construction of these chiral honeycombs is described along with the simulation methodology used and experimental testing coupled with digital image correlation (DIC) analysis of these metamaterials.

2.1 Geometry of chiral honeycombs

The chiral systems investigated in this work are illustrated in Figure 2. These metamaterials were designed by the chiralisation of two 2D multi-polygonal tessellations exhibiting

rotational symmetry of order 6 and their dual counterparts. The dual tessellations are derived directly from the original base tessellations through the formation of vertices at the centre points of the polygons which are connected together through lines bisecting the sides of the original tessellation. As a result of this, the dual systems are monohedral tiling variants of the original tessellations and retain the same symmetry characteristics (Grünbaum and Shephard 1977, 2016). The four tessellations studied in this work are denoted according to Conway's nomenclature (Conway *et al.*, 2008), which lists these systems as follows: the Rhombi-Trihexagonal (RT) tiling with its corresponding dual tessellation being the Deltoid-Trihexagonal (DT) and the Snub-Trihexagonal (ST) with its Florent Pentagonal (FP) dual equivalent. The chiral systems based on these tessellations are designed according to the following independent geometric parameters: the radius of the chiral node, r, the thickness of the ligament, t, and the side length of the original tessellation, p. In addition, to allow for a more accurate analysis of the localised stress concentrations and failure modes, the connection between the ligaments and the chiral nodes was rounded up with a circular fillet of radius, r_f.

To obtain a complete picture of the mechanical behaviour of these systems, the following geometric parameters were used for each of the four structures (Table 1). These values were chosen on the basis of the results of linear, periodic simulations in work previously conducted by the same authors (Mizzi and Spaggiari, 2021) and encompass systems with the potential to exhibit a negative, positive and *quasi*-zero Poisson's ratios. Furthermore these systems are also transversely-isotropic which means that their deformation mode can be analysed independently of the uniaxial loading orientation.

Figure 2 Diagram showing the four tessellations and their chiralised counterparts

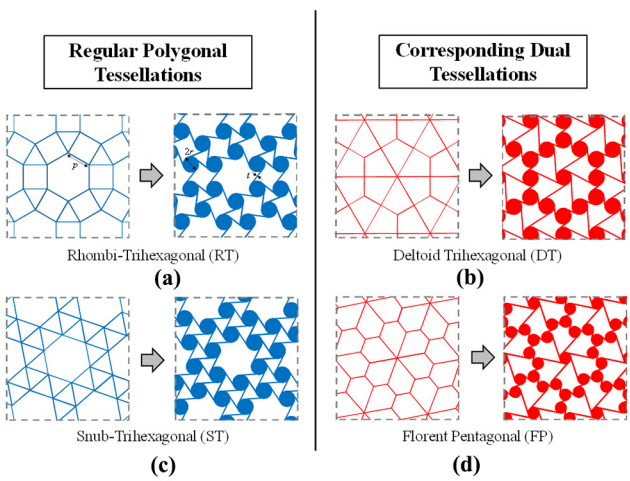

Notes: (a) Rhombi-trihexagonal (RT); (b) deltoid trihexagonal (DT); (c) snub-trihexagonal (ST); (d) florent pentagonal (FP); the geometric parameters p, r and t are also indicated
Source: Authors' own work

Table 1 Geometric parameters of the four chiralised tessellations studied and the resultant unit cell dimensions in the x and y-directions (l_x and l_y)

System	p (mm)	r (mm)	t (mm)	r_f (mm)	l_x (mm)	l_y (mm)
RT	15	4.5	0.9	0.2	40.98	70.98
DT	15	4.5	0.9	0.2	40.98	70.98
ST	15	3.7	0.9	0.2	39.68	68.74
FP	15	3.7	0.9	0.2	39.68	68.74

Source: Authors' own work

2.2 Finite element simulations

To analyse the high-strain deformation of these systems, a number of FE simulations were conducted using the ANSYS16 software. The chiral honeycombs were built as 2 D systems and meshed using the PLANE183 element; an eight-node quadratic element with two degrees of freedom. Following mesh convergence tests, a minimum mesh size of $t/4$ was used for each system simulated. The linear material properties of Acrylonitrile Butadiene Styrene (ABS) plastic were used, as listed in the material data sheet (Stratasys, 2017); the Young's modulus was set to 2,200 MPa while a Poisson's ratio of 0.3 was used.

Two types of boundary conditions were used to analyse these systems. The first set of simulations were conducted on a single representative unit cell under periodic boundary conditions (PBC). This was done to investigate the influence of high-strain deformation independently of edge effects. As these systems do not possess an axis of mirror symmetry, PBC were implemented through the use of constraint equations applied to the nodes at the edges of the unit cell. These constraint equations [equations (1) and 2] involve four nodes and couple the displacements of two master nodes ($U_{1,\text{master}}$ and $U_{2,\text{master}}$); each corresponding to one other on opposing edges; with those of a pair of slave nodes on the same edges ($U_{1,\text{slave}}$ and $U_{2,\text{slave}}$) and ensure that the deformations at the edge of the unit cell are replicated on each pair of opposing edges. As shown in Figure 3(a), the system was pinned from one node on the bottommost edge and fixed in the x-direction from the corresponding opposing node at the topmost edge to retain alignment of unit cell with the y-axis during deformation. A compressive strain of 5% in the y-direction was applied on the latter node to induce deformation. This loading mode and method for implementing PBC is based on the theoretical work of Suquet (Suquet, 1987) and has been validated and explained in greater detail in (Mizzi *et al.*, 2021):

$$Ux_{1,master} - Ux_{2,master} - Ux_{1,slave} + Ux_{2,slave} = 0 \quad (1)$$

$$Uy_{1,master} - Uy_{2,master} - Uy_{1,slave} + Uy_{2,slave} = 0 \quad (2)$$

The second set of simulations, on the other hand, was conducted under loading conditions which are analogous to experimental tests using a loading machine where a sample is placed between two rigid plates and compressed. In this case, finite systems consisting of multiple unit cells (5×3 representative unit cells in the x- and y-directions respectively) were used. The systems were fixed in the x- and y-direction from the bottommost edge while the right and left edges of the

Figure 3 Demonstration of the boundary and loading conditions used for the (a) periodic and (b) finite simulations of these systems (Structure Deltoid Trihexagonal [DT] shown here)

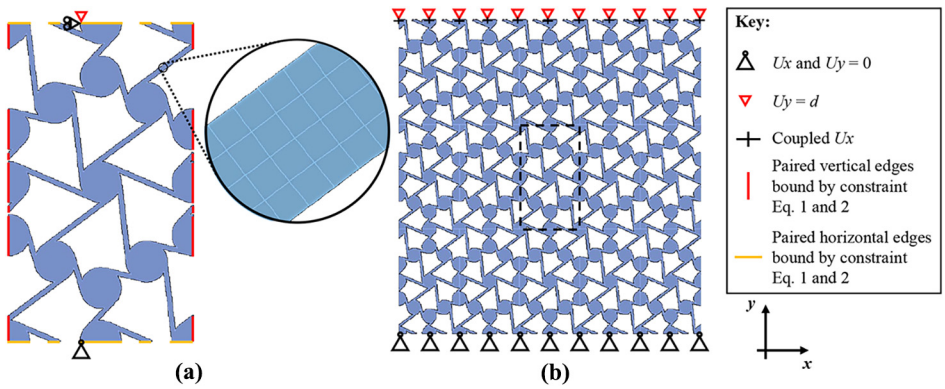

Notes: The dashed central box in (b) indicates the representative unit cell from which the Poisson's ratio was measured; a close-up of the mesh on a ligament is also provided in (a)
Source: Authors' own work

system were left free and unconstrained, as shown in Figure 3(b). A displacement, d, equivalent to −0.08% global strain was applied on the topmost edge nodes. In addition to this, the nodes on the topmost edge were constrained using coupling equations to maintain the same displacement in the x-direction during deformation. This condition was applied to allow for the fact that while in the experimental samples (shown in Figure 4) the upper surface of the system is fixed to a block of material and thus is constrained, the entire surface as a whole is allowed to shift in the x-direction during deformation and lose its alignment to the y-axis with respect to the bottom layer. As discussed later on in the results and discussion section, this mode of deformation was observed for some of the experimental samples during loading. The Poisson's ratio of the systems was measured from the centremost unit cell. This was done by measuring the displacements of the nodes on the border of the unit cell, finding the average strains in the x- and y-directions and, finally, calculating the engineering Poisson's ratio. Both sets of simulations were conducted under non-linear geometric loading conditions with large deflections allowed and a minimum number of 100 substeps.

2.3 Experimental tests

Four samples corresponding to the finite element simulations with realistic boundary conditions were additively manufactured in ABS using a Stratasys Fortus 250mc FDM printer. The CAD models were extruded by 20 mm in the z-direction and rectangular blocks of material were added to the uppermost and lowermost edges to be able to affix the test sample to the tensile loading machine. The four samples, shown in Figure 4(a–d), were manufactured in ABSPlus using the double-wall method with a contour width of 0.5080 mm and raster angles of −45°/0°/45°/90°. The printing infill density was set to sparse-high (over 95% infill) and the slice height at 0.2540 mm. The nozzle and print chamber temperatures were set at 280° and 75°, respectively. Before testing, the additively manufactured samples were spray-painted with a black and white speckle pattern in preparation for the DIC analysis. The samples were mounted on a Galdabini® Sun500 universal tensile machine with a 250 N loadcell as shown in Figure 4(e). As the samples were considerably large in size, instead of using circular rigid plates to directly compress the border of the samples, rigid rectangular metal bars were placed between the plates and the sample to ensure that the load is uniformly applied to the upper area of the samples. In each case, two tests were conducted. In the first test, a compressive displacement of 8 mm (equivalent to about 4% global strain) was applied to the additively-manufactured prototype at a rate of 5 mm/min, followed by a return to the rest position at the same load rate. In the second test, a compressive displacement of 25 mm was applied at a displacement rate of 10 mm/min to observe the failure modes of the systems. This displacement is equivalent to a high global compressive strain of about 12.5%.

To measure the Poisson's ratios of these systems, a Dantec Q-400 DIC software was used. An optical camera was focused on the central unit cell of the additively-manufactured prototypes and the deformation of the system during loading was recorded. Due to the high level of porosity and the large localised displacements of these systems during deformation, a point-tracking DIC analysis was used rather than a full-field displacement method. Using the Istra3D® software, various points on the unit cell were tracked, as shown in Figures 4(f) and (g), at an interval of 1 Hz and these displacements were used to calculate the strains and Poisson's ratio. In the case of the dual tessellations (DT and FP), the four corners of the unit cell were tracked, while in the case of the original tessellations (RT and ST), sixteen points at the border of the unit cell were tracked since the systems have pores at the corner of the cell. In both cases, for n pairs of points at the edges of the unit cell, the strains and Poisson's ratio were calculated as follows:

$$\overline{\varepsilon}_x = \frac{\sum_{i=1}^{n}\left[\frac{(ix_{t,right} - ix_{t,left}) - (ix_{0,right} - ix_{0,left})}{(ix_{0,right} - ix_{0,left})}\right]}{n} \quad (3)$$

Figure 4 Images showing the additively manufactured prototypes and DIC point-tracking analysis

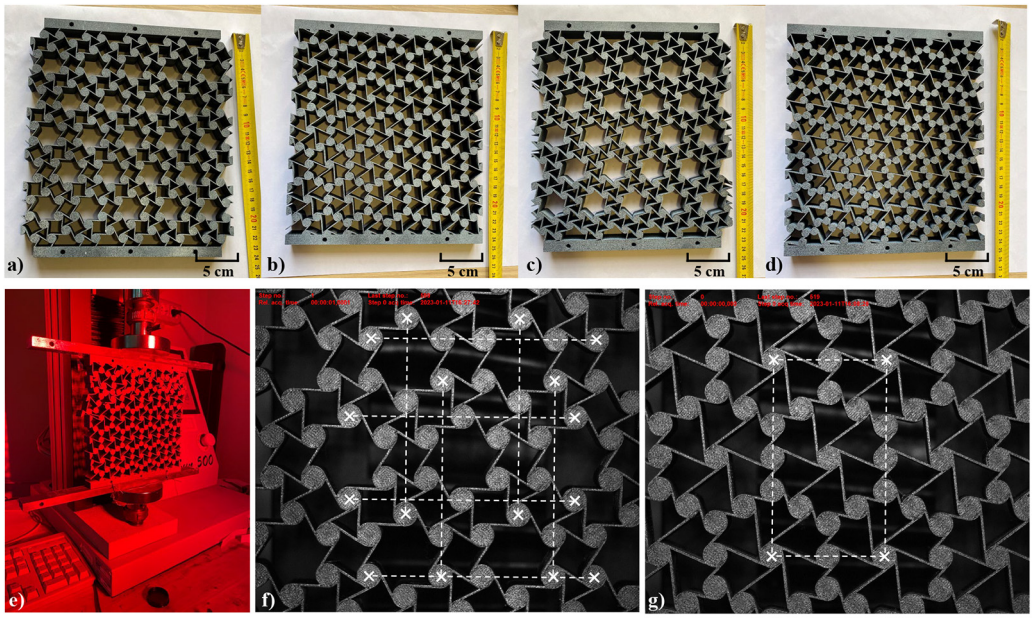

Notes: (a) Rhombi trihexagonal (RT); (b) deltoid trihexagonal (DT); (c) snub trihexagonal (ST); (d) florent pentagonal (FP) 5×3 samples with the painted speckle pattern; (e) photo showing the DT sample mounted on the loading machine under LED light in preparation for the DIC analysis; diagrams (f); (g) show the black and white close-up images of the central representative unit cells of the RT and DT prototypes, respectively; the white crosses indicate the points tracked by DIC and the dotted lines the length used to measure the strains. Note that as there are no chiral nodes at the corner of the cell in RT (f), multiple points were tracked and averaged to find the strain of the representative cell (as DIC-tracking is most accurate at the chiral nodes rather than the ligaments) and, for the x-direction, the strain was calculated over the length of two unit-cells to account for the deviation from the central position of the chosen points. An analogous approach was used for the RT and DT systems
Source: Authors' own work

$$\overline{\varepsilon}_y = \frac{\sum_{i=1}^{n}\left[\frac{(iy_{t,top} - iy_{t,bottom}) - (iy_{0,top} - iy_{0,bottom})}{(iy_{0,top} - iy_{0,bottom})}\right]}{n} \quad (4)$$

$$\nu_{yx} = -\frac{\overline{\varepsilon}_x}{\overline{\varepsilon}_y} \quad (5)$$

where $ix_{t,right}$ and $ix_{t,left}$ represent the x-coordinates of the rightmost and leftmost edge points respectively at time t, $iy_{t,top}$ and $iy_{t,bottom}$ represent the y-coordinates of the topmost and bottommost edge nodes respectively at time/step number t and the corresponding $ix_{0,right}$, $ix_{0,left}$, $iy_{0,top}$ and $iy_{0,bottom}$ variables represent the initial coordinates of the same points at $t = 0$. This approach is analogous to the method used to calculate the Poisson's ratio of the central unit cell from the Finite Element simulations with realistic, finite boundary conditions.

The engineering stress-strain plots were also extracted and analysed. In the case of the experimental samples and simulations on finite systems, the strains and stresses were calculated globally for the system as a whole, rather than considering solely the central unit cell as in the case of the Poisson's ratio. Therefore, for the experimental samples, the displacements used to calculate the engineering strains as well as the forces used to find the stresses, were obtained directly from the output of the tensile loading machine. An analogous method was also used to extract this data from the simulations on the finite systems.

3. Results and discussion

In the first part of this section, the results obtained from the non-linear simulations and experimental results for loading up to 3% compressive strain are presented and analysed in terms of Poisson's ratio, stiffness and deformation behaviour. This is followed by an analysis of the observations of the high strain compressive loading tests up to failure in the second part of the discussion.

3.1 Low-strain compressive loading

A comparison of the Poisson's ratios obtained from the two sets of FE simulations and the experimental tests on the additively-manufactured samples is plotted in Figure 5, while images showing the undeformed and deformed forms of each chiral system are shown in Figure 6. Note that for the FP system a lower compressive strain threshold is used in comparison to the other chiral honeycombs; i.e. *circa* −0.017; as the system underwent failure at this strain level. The Poisson's ratios and Young's moduli are listed in Table 2.

Figure 5 Plots showing the changes in engineering Poisson's ratio with increasing compressive engineering strain obtained from the Periodic FE simulations, the simulations on Finite systems with realistic boundary conditions and the DIC analysis of the experimental tests on the additively-manufactured structures

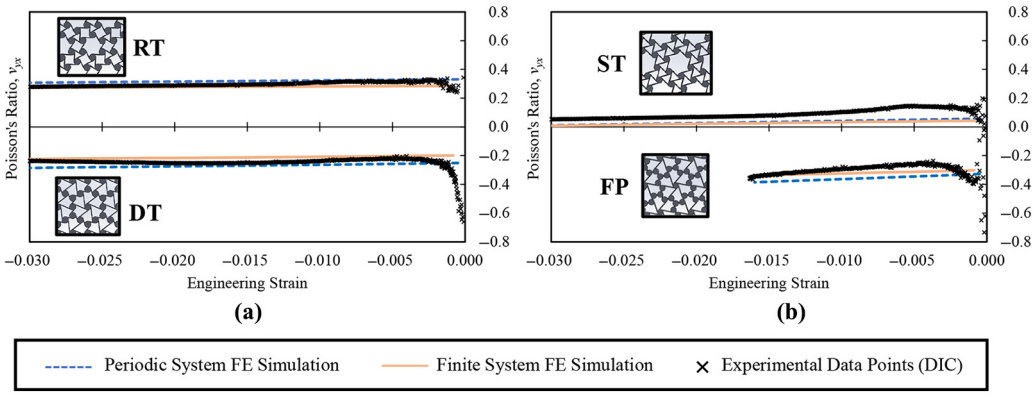

Source: Authors' own work

Figure 6 Images showing the central RUC of the undeformed experimental system and the deformed experimental and simulation systems (both finite and periodic)

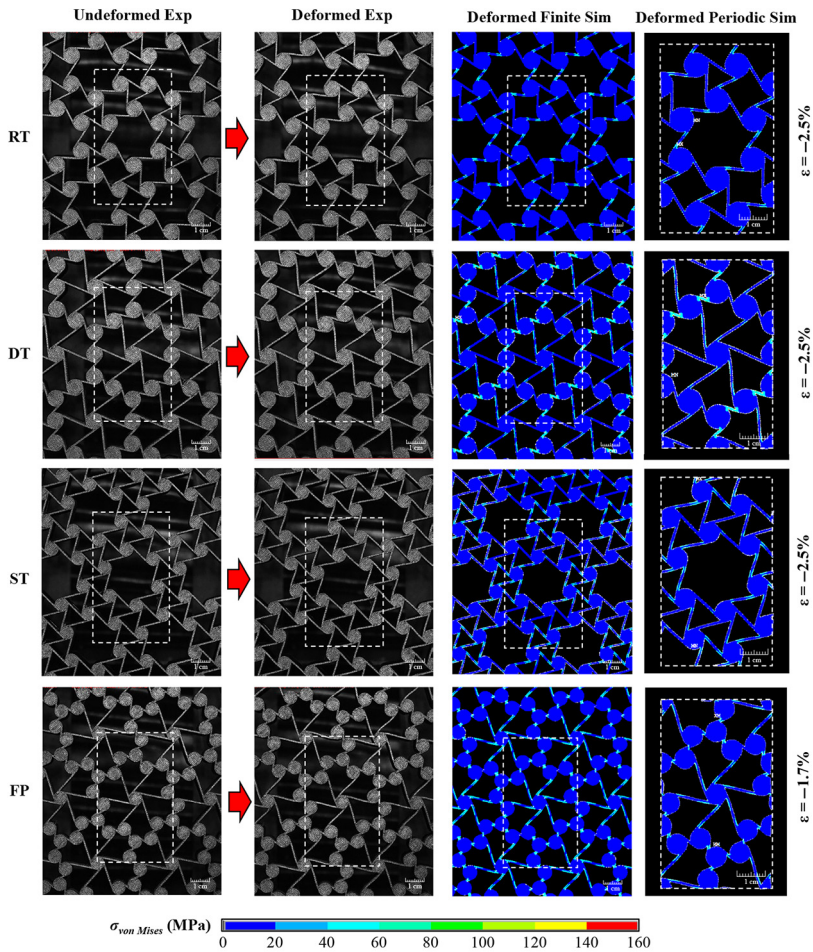

Notes: The von Mises stress distributions are indicated on the simulation results. The dashed white lines indicate the unit cell from which the Poisson's ratio was measured in each case
Source: Authors' own work

Table 2 Small-strain (linear) Poisson's ratios and Young's moduli obtained from the periodic and finite simulations as well as the experimental tests over a strain range of −0.03

	Periodic simulation		Finite simulation		Experimental tests	
System	ν	***E*** **(MPa)**	ν	***E*** **(MPa)**	ν	***E*** **(MPa)**
RT	+0.319	6.907	+0.233	7.535	+0.283	6.131
DT	−0.269	28.019	−0.233	23.262	−0.246	12.794
ST	+0.033	11.955	+0.048	11.904	+0.148	9.902
FP	−0.382	30.681	−0.227	26.890	−0.318	16.226

Source: Authors' own work

It is evident from the Poisson's ratio plots in Figure 5 that the results obtained from both sets of simulations and the experimental tests show extremely good agreement. In the case of both dual tessellation-based systems DT and FP, negative Poisson's ratio behaviour in the range of −0.2 and −0.4 is observed over a 3% compressive strain range. On the other hand, the RT chiral system exhibits a positive Poisson's ratio of +0.3 which is constant over the considered strain range. Lastly, the ST system, which is predicted by both finite and periodic simulations to exhibit a *quasi*-zero Poisson's ratio (+0.03), was experimentally shown to exhibit a low positive Poisson's ratio of +0.12 up to −1% strain which gradually becomes lower with increasing compressive strain, approaching the zero value. Furthermore, it is apparent, both from the plots in Figure 5 and the deformation profiles shown in Figure 6, that the influence of edge effects on the mechanical behaviour of these systems is minimal. This is indicated by the fact that the periodic simulations and the central cell of the realistic boundaries simulations show almost identical localised stress distributions and contours. This factor is characteristic of many auxetic chiral metamaterials (Mizzi *et al.*, 2018a, 2018b; Mizzi *et al.*, 2020b), and it is evident that this class of structures also possesses this advantageous property.

The deformation profiles shown in Figure 6 also present a number of points of interest. It is clear that in the dual systems (DT and FP), the main deformation mode is rotation of the chiral node attached to six ligaments and flexure of these ligaments. This deformation mechanism typically results in a negative Poisson's ratio, as is the case for these two systems. On the other hand, the other two chiral metamaterials do not show any rotations of the chiral nodes and in both cases the stresses and deformations are mainly localised along the ligaments of the "hexagonal" pore which are almost vertically aligned. This means that the chiral/rotating mechanism which leads to auxetic behaviour is absent, resulting in non-auxetic behaviour.

The engineering stress-strain plots obtained from the experimental and simulation results are presented in Figure 7, while the average stiffnesses are shown in Table 2. As stated earlier in the methodology section, in the former case these values were obtained directly from the output of the tensile loading machine, while an analogous method was used for the simulation results. This means that the stresses and strains obtained from the experimental and finite (non-periodic) simulations are actually the apparent stresses and strains obtained from the average deformation of all the representative unit cells making up the entire tested samples. Furthermore, this means that in the case of System FP, the global engineering strain at failure was equal to −0.032, rather than −0.017 as in the case of the analysis of the central representative unit cell shown in Figure 5(b).

It is evident from the plots in Figure 7 that the dual tessellation-based chiral systems, ST and FP, exhibit a higher level of stiffness relative to the RT and DT chiral honeycombs. This finding was to be expected as there is significant deformation of short, thick ligaments in the former systems, as shown in Figure 6, which are considerably stiffer than the longer ligaments found in the RT and DT systems. Moreover, in the latter chiral honeycombs, the deformation of the system upon loading is absorbed by a specific number of ligaments while the rest remain relatively undeformed, hence resulting in an overall lower stiffness for the entire system.

It is also apparent, that while there is good agreement between the FE simulation predictions and the experimental results in the case of the original tessellation-based systems RT and DT, the simulations overestimate the stiffness of the dual-based chiral systems ST and FP by a significant degree. This is probably due to the fact that in the simulations, the localised stresses are more or less uniformly distributed throughout the various representative unit cells making up the system (as shown in Figure 6), while in reality the presence of any structural imperfections or asymmetries in certain ligaments, however minute, will lead to a more uneven distribution of localised stress, weakening the system. It has been shown, in previous studies on other chiral honeycombs, that the stiffness of auxetic chiral systems with a relatively low number of degrees of freedom is greatly influenced by the presence of defects, even in the form of small imperfections while the Poisson's ratio can remain almost unchanged (Mizzi *et al.*, 2015). The dual systems ST and FP can also be considered to fall under this classification and, therefore, it is possible that these discrepancies between simulation and experimental results in terms of stress-strain behaviour may be due to the same reasons, although further studies are required to confirm this. Nonetheless, this hypothesis could also explain why such good agreement was observed in the case of the RT and DT systems. As the localised stresses are already predicted from the simulations to be less uniformly distributed and are concentrated on a specific set of ligaments, the influence of minor random asymmetries or imperfections throughout the structure should be minimal on the global response of the metamaterial system since they do not alter the localised stress distribution profile of the overall system in a significant manner.

3.2 High-strain compressive loading

The stress-strain plots obtained from the high strain compressive loading tests on the experimental samples are presented in Figure 8. In the case of the system RT, the test was stopped at a smaller strain value than the other samples (about 4%, equivalent to 8 mm displacement) due to the fact that the system underwent failure

Figure 7 Plots showing the changes in global engineering stress with global engineering strain up to −0.03 obtained from the Periodic FE simulations, the simulations on Finite systems with realistic boundary conditions and the tensiometer data for the experimental tests on the additively manufactured structures

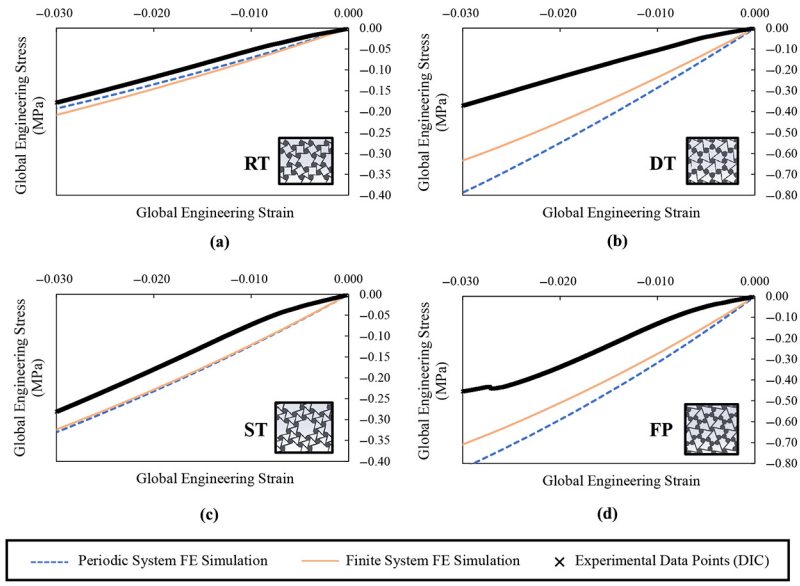

Source: Authors' own work

Figure 8 Stress-strain plots obtained from the experimental tests on the additively manufactured samples

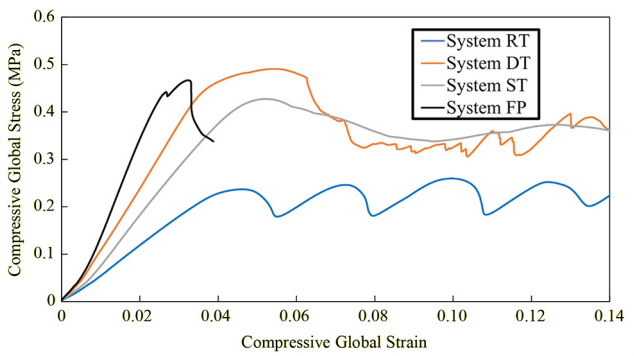

Source: Authors' own work

with multiple fracture points at this stage. The other systems were compressed up to a strain of 14%–16%.

It is clear from Figure 8 that all the chiral structures except System FP underwent their first irreversible failure at a compressive displacement of about 5%. This value is significantly lower than the compressive strain failure limit of 3D-printed ABS (Dominguez-Rodriguez *et al.*, 2018) due to the presence of regions of high localised stress concentrations (Figure 6). Despite possessing similar a similar failure strain threshold, the dual and original tessellation-based chiral systems were characterised by a considerably different fracture propagation profile. The failure of the dual tessellations was observed to be extremely localised to two distinct regions; namely the upper right and left corners of the test sample; with the rest of the structure showing very damage. These regions where outside the target area used for acquisition of images for the DIC analysis of the small-strain compressive behaviour. An image of the sample DT after testing is shown in Figure 9, with zoomed-in images of the main failure zones.

This deformation profile differs significantly from that predicted by the FE simulation at small strains on the finite corresponding structure, where the localised stresses are distributed more or less equally between the uppermost and lowermost layers of representative unit cells. This difference can most probably be attributed to localised defects/asymmetries which result in a localisation of the deformation to one side of the structure rather than a more symmetrical distribution. Although no visible major defects were observed on the prototype prior to testing, minute defects could still give rise to this effect, and it has been shown in other studies found in the literature (Coukir and Singh, 2023; Jiang *et al.*, 2022;

Figure 9 Image of chiral system deltoid trihexagonal (DT) after the application of a compressive displacement stroke of 25 mm showing the failure regions and the directions from which the fracture initiated and propagated within the system

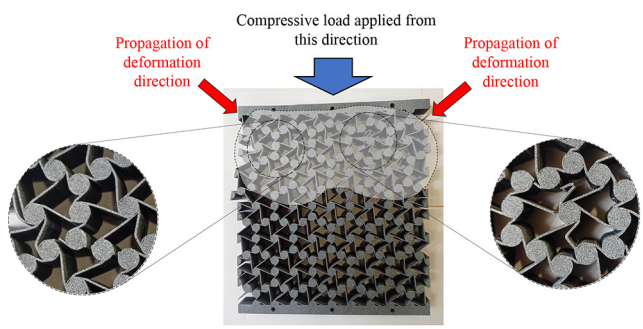

Source: Authors' own work

Wang *et al.*, 2021) that even highly symmetric metamaterial systems still tend to undergo fracture/failure in an asymmetric manner despite the use of high printing resolution. As mentioned in the previous section, this explanation could also account for the fact that the FE simulations overestimate the stiffness of these systems.

On the other hand, the systems RT and ST were characterised by distinctly different failure and fracture propagation profiles – a sequential layer by layer collapse of representative unit cells row by row. This is particularly evident for the system RT, shown in Figure 10, where the force-displacement plot is also characterised by a series of peaks and valleys with each representing the failure of an entire row of ligaments. The collapse started from the bottommost row of representative unit cells and, interestingly enough, only the ligaments of the hexagonal pore aligned along the loading direction collapsed while the rest of the ligaments underwent very little deformation. These ligaments were highlighted from both the periodic and non-periodic simulations shown in Figure 6 as being the regions of maximum localised stress concentration, so the failure of these ligaments first was to be expected. However, the propagation of fracture of ligaments is still somewhat anomalous. Typically, in metamaterial systems which are characterised by sequential layer-by-layer collapse such as re-entrant hexagonal honeycombs (Zhang and Lu, 2023; Zhang *et al.*, 2020), the instable collapse of one layer in a particular direction is followed by the collapse of the next layer in the opposite

Figure 10 (a) Sequential images showing the initial state of the central region of the sample taken by the camera used for the DIC analysis of system Rhombi Trihexagonal (RT) and the 2nd, 3rd and 4th layer collapses as the loading test progressed (the first collapse occurred outside the region on which the camera was focused and thus images are not available); (b) force-displacement plot of system RT showing the collapse points from which the images in a) were taken; (c) test sample after the loading test was completed and the sample removed from the loading machine showing the collapsed ligament layers

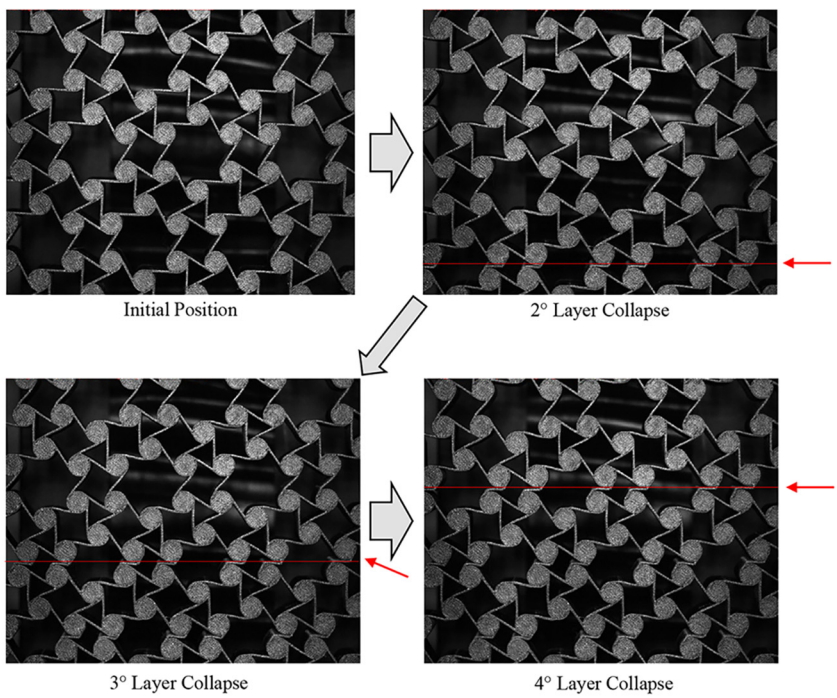

(a)

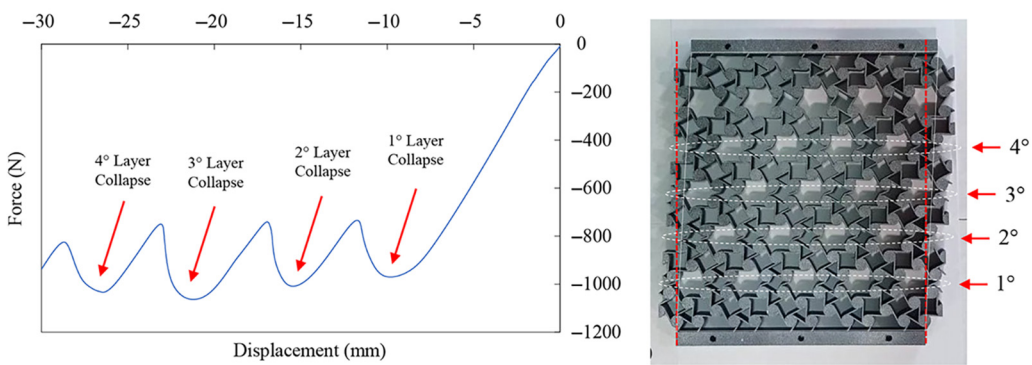

(b) (c)

Source: Authors' own work

direction. In this case, however, the direction of collapse is directed by the chirality of the metamaterial system and thus the ligaments always collapse in the same direction. This leads to a shearing deformation of the system as shown in Figure 10(c). In addition, the layers of collapsed ligaments are not adjacent to each other but are separated by other ligaments which deform very little in comparison.

A similar effect, but much less pronounced, was observed for System ST. In this case, a layer-by-layer collapse also occurred, however the collapse of each layer was less clear-cut than in the case of System RT, as also evidenced by the plot shown in Figure 8. In Figure 11, images of the central region of the experimentally tested samples are shown, before and after complete loading (at −25 mm applied displacement). It is clear that even in this case, system failure occurs mainly along the "vertically" aligned ligaments of the hexagonal pore. This is also in accordance with the predictions of the FE simulations shown in Figure 6.

Before concluding, it is important to note that in this work we have examined experimentally for the first time the deformation types and failure modes of this new class of chiral metamaterials and the main aim of this study was to obtain a preliminary outlook of the high-strain behaviour of these structures. Our findings indicate that besides being able to exhibit a reasonably good range of Poisson's ratios including positive, zero and negative values, these systems possess anomalous fracture propagation and failure modes which are of great interest and merit further study. These unusual failure modes are probably the result of the complex representative unit cell of these systems which is relatively larger and has considerably more structural elements than typical metamaterials based on regular monohedral tessellations, thus giving rise to greater localised stress dispersions within the representative cell itself and non-uniform deformations. Auxetic metamaterials, thanks to the ease of manufacture provided by additive manufacturing, have already been proposed as potential candidates for applications involving impact resistance and energy absorption (including sports equipment and vehicular crash-protection components), and thus, it is possible that these new chiral systems could be used for similar purposes in the future, particularly if the fracture propagation and deformation pathway can be controlled as a function of geometry. This could potentially be achieved in the future through the employment of geometric optimisation techniques using traditional optimisation algorithms or even generative design/deep learning-based methods to produce functionally graded chiral systems with pre-determined, controlled failure modes guided through the grading of the metamaterial geometry. However, further work is necessary to achieve this level of advanced functionalities and more studies need to be carried out on the high-strain behaviour of other Euclidean tessellation-based chiral systems and on localised fracture modes occurring throughout the metamaterial systems.

Figure 11 Image showing the ST system before and after loading

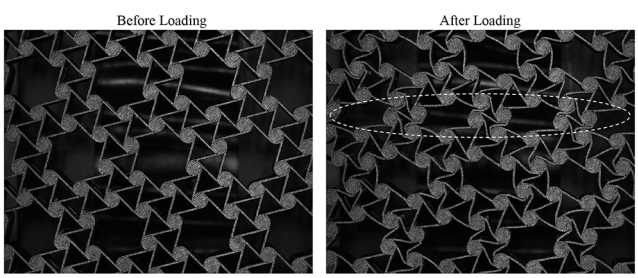

Note: The white dotted line indicates the layer of collapsed ligaments
Source: Authors' own work

4. Conclusions

In this work, four new chiral metamaterial structures based on 2D Euclidean polygonal tessellations were designed, additively manufactured and analysed through a combination of experimental tests and FE simulations. The low-strain and high-strain performance of these systems was investigated using DIC analysis to measure the Poisson's ratio and observe the fracture and failure modes. The results obtained indicate that these systems have the ability to exhibit positive, zero and negative Poisson's ratios and also showed that the dual tessellation-based systems (Deltoid Trihexagonal and Florent Pentagonal) are characterised by a higher level of stiffness in comparison to their original multi-polygonal tessellation counterparts (Rhombi Trihexagonal and Snub Trihexagonal). The dual systems also exhibited failure modes which were characterised by a large density of fractured ligaments in two particular regions of the global system while the original tessellation-based chiral systems showed failure profiles which can be described as a sequential layer-by-layer collapse of ligaments within the system. The direction of collapse in the latter systems was also found to be uni-directional, as a consequence of the chirality of the system, thus resulting in shearing of the system despite the application of a monoaxial load. This work shows that this new class of chiral metamaterials, besides being extremely versatile and having the ability to exhibit a wide range of mechanical properties, may also possess a number of additional advantageous and potentially useful properties related to energy absorption and impact resistance as well, which may differ considerably from those found in typical regular monohedral tessellation-based metamaterials.

References

Airoldi, A., Bettini, P., Panichelli, P., Oktem, M.F. and Sala, G. (2015), "Chiral topologies for composite morphing structures – part I: development of a chiral rib for deformable airfoils", *Physica Status Solidi (b)*, Vol. 252 No. 7, pp. 1435-1445, doi: 10.1002/pssb.201451689.

Alderson, A., Alderson, K.L., Attard, D., Evans, K.E., Gatt, R., Grima, J.N., Miller, W., Ravirala, N., Smith, C.W. and Zied, K. (2010), "Elastic constants of 3-, 4- and 6-connected chiral and anti-chiral honeycombs subject to uniaxial in-plane loading", *Composites Science and Technology*, Vol. 70 No. 7, pp. 1042-1048, doi: 10.1016/j.compscitech.2009.07.009.

Bacigalupo, A. and De Bellis, M.L. (2015), "Auxetic anti-tetrachiral materials: equivalent elastic properties and frequency band-gaps", *Composite Structures*, Vol. 131, pp. 530-544, doi: 10.1016/j.compstruct.2015.05.039.

Bacigalupo, A. and Gambarotta, L. (2014), "Homogenization of periodic hexa- and tetrachiral cellular solids", *Composite Structures*, Vol. 116 No. 1, pp. 461-476, doi: 10.1016/j.compstruct.2014.05.033.

Bacigalupo, A. and Gambarotta, L. (2020), "Chiral two-dimensional periodic blocky materials with elastic interfaces: auxetic and acoustic properties", *Extreme Mechanics Letters*, Vol. 39, p. 100769, doi: 10.1016/j.eml.2020.100769.

Bertoldi, K., Vitelli, V. and Christensen, J. (2017), "Flexible mechanical metamaterials", *Nature Reviews*, Vol. 2, p. 17066. doi: 10.1038/natrevmats.2017.66.

Chen, Y.J., Scarpa, F., Liu, Y.J. and Leng, J.S. (2013), "Elasticity of anti-tetrachiral anisotropic lattices", *International Journal of Solids and Structures*, Vol. 50 No. 6, pp. 996-1004.

Chow, L., Yick, K.L., Wong, K.H., Leung, M.S.H., Sun, Y., Kwan, M.Y., Ning, K., Yu, A., Yip, J., Chan, Y.F. and Ng, S.P. (2022), "3D printing auxetic architectures for hypertrophic scar therapy", *Macromolecular Materials and Engineering*, Vol. 307 No. 5, p. 2100866.

Conway, J.H., Burgiel, H. and Goodman-Strauss, C. (2008), "'Archimedean 'tilings", in Peters, A.K. (Ed.), *The Symmetry of Things*, CRC Press, New York.

Coukir, S. and Singh, C.V. (2023), "Role of topology in dictating the fracture toughness of mechanical metamaterials", *International Journal of Mechanical Sciences*, Vol. 241, p. 107945.

Dominguez-Rodriguez, G., Ku-Herrera, J.J. and Hernandez-Perez, A. (2018), "An assessment of the effect of printing orientation, density and filler pattern on the compressive performance of 3D-printed ABS structures by fuse deposition", *The International Journal of Advanced Manufacturing Technology*, Vol. 95 Nos 5/8, pp. 1685-1695.

Dudek, K.K., Iglesias-Martinez, J.A., Ulliac, G. and Kadic, M. (2022), "Micro-scale auxetic hierarchical mechanical metamaterials for shape morphing", *Advanced Materials*, Vol. 34 No. 14, p. 2110115.

Dudek, K.K., Mizzi, L., Iglesias-Martinez, J.A., Spaggiari, A., Ulliac, G., Gatt, R., Grima, J.N., Laude, V. and Kadic, M. (2023), "Micro-scale graded mechanical metamaterials exhibiting versatile poisson's ratio", *Composite Structures*, Vol. 319, p. 117151, doi: 10.1016/j.compstruct.2023.117151.

Duncan, O., Shepherd, T., Moroney, C., Foster, L., Venkatraman, P.D., Winwood, K., Allen, T. and Alderson, A. (2018), "Review of auxetic materials for sports applications: expanding options in comfort and protection", *Applied Sciences*, Vol. 8 No. 6, doi: 10.3390/app8060941.

Evans, K.E., Nkansah, M.A., Hutchinson, I.J. and Rogers, S.C. (1991), "Molecular network design", *Nature*, Vol. 353 No. 6340, p. 124.

Grima, J.N. and Evans, K.E. (2000), "Auxetic behavior from rotating squares", *Journal of Materials Science Letters*, Vol. 19 No. 17, pp. 1563-1565.

Grima, J.N. and Evans, K.E. (2006), "Auxetic behavior from rotating triangles", *Journal of Materials Science*, Vol. 41 No. 10, pp. 3193-3196, doi: 10.1007/s10853-006-6339-8.

Grima, J.N., Alderson, A. and Evans, K.E. (2005), "Auxetic behaviour from rotating rigid units", *Physica Status Solidi (B)*, Vol. 242 No. 3, pp. 561-575, doi: 10.1002/pssb.200460376.

Grima, J.N., Gatt, R. and Farrugia, P.S. (2008), "On the properties of auxetic meta-tetrachiral structures", *Physica Status Solidi (b)*, Vol. 245 No. 3, pp. 511-520, doi: 10.1002/pssb.200777704.

Grünbaum, B. and Shephard, G.C. (1977), "Tilings by regular polygons", *Mathematics Magazine*, Vol. 50 No. 5, pp. 227-247, doi: 10.1080/0025570X.1977.11976655.

Grünbaum, B. and Shephard, G.C. (2016), *Tillings and Patterns*, 2nd edn. Dover Publications, New York.

Hassan, M.R., Scarpa, F., Ruzzene, M. and Mohammed, N.A. (2008), "Smart shape memory alloy chiral honeycomb", *Materials Science and Engineering: A*, Vols 481/482 Nos 1/2 C, pp. 654-657, doi: 10.1016/j.msea.2006.10.219.

Hu, L.L., Ye, W.K. and Wu, Z.J. (2019), "Mechanical property of anti-trichiral honeycombs under large deformation along the x-direction", *Thin-Walled Structures*, Vol. 145, p. 106415, doi: 10.1016/j.tws.2019.106415.

Jacobs, S., Coconnier, C., DiMaio, D., Scarpa, F., Toso, M. and Martinez, J. (2012), "Deployable auxetic shape memory alloy cellular antenna demonstrator: design, manufacturing and modal testing", *Smart Materials and Structures*, Vol. 21 No. 7, doi: 10.1088/0964-1726/21/7/075013.

Jang, B., Won, S., Kim, J., Kim, J., Oh, M., Lee, H.J. and Kim, J.H. (2022), "Auxetic meta-display: stretchable display without image distortion", *Advanced Functional Materials*, Vol. 32 No. 22, p. 2113299.

Jiang, F., Yang, S. and Qi, C. (2022), "Quasi-static crushing response of a novel 3D re-entrant circular auxetic metamaterial", *Composite Structures*, Vol. 300, p. 116066.

Kaur, M. and Kim, W.S. (2019), "Toward a smart compliant robotic gripper equipped with 3D-designed cellular", *Advanced Intelligent Systems*, Vol. 1 No. 3, p. 1900019.

Lee, Y.J., Misra, S., Chen, W.H., Koditschek, D.E., Sung, C. and Yang, S. (2021), "Tendon-Driven auxetic tubular springs for resilient hopping robots", *Advanced Intelligent Systems*, Vol. 4 No. 4, p. 2100152.

Linforth, S., Ngo, T., Tran, P., Ruan, D. and Odish, R. (2021), "Investigation of the auxetic oval structure for energy absorption through quasi-static and dynamic experiments", *International Journal of Impact Engineering*, Vol. 147 No. 2020, p. 103741, doi: 10.1016/j.ijimpeng.2020.103741.

Masters, I.G. and Evans, K.E. (1996), "Models for the elastic deformation of honeycombs", *Composite Structures*, Vol. 35 No. 4, pp. 403-422.

Mizzi, L., Attard, D., Gatt, R., Farrugia, P.S. and Grima, J.N. (2018a), "An analytical and finite element study on the mechanical properties of irregular hexachiral honeycombs", *Smart Materials and Structures*, Vol. 27 No. 10, p. 105016.

Mizzi, L., Mahdi, E.M., Titov, K., Gatt, R., Attard, D., Evans, K.E., Grima, J.N. and Tan, J.C. (2018b), "Mechanical metamaterials with star-shaped pores exhibiting negative and zero poisson's ratio", *Materials & Design*, Vol. 146, pp. 28-37.

Mizzi, L., Salvati, E., Spaggiari, A., Tan, J.C. and Korsunsky, A.M. (2020a), "2D auxetic metamaterials with tuneable micro-/nanoscale apertures", *Applied Materials Today. Elsevier Ltd*, Vol. 20, p. 100780, doi: 10.1016/j.apmt.2020.100780.

Mizzi, L., Sorrentino, A., Spaggiari, A. and Castagnetti, D. (2020b), "A comparison between rotating squares and anti-tetrachiral systems: influence of ligaments on the multi-axial mechanical response", *Proceedings of the Institution of Mechanical Engineers Part C: Journal of Mechanical Engineering Science*, Vol. 235 No. 24, pp. 7759-7773.

Mizzi, L., Grasselli, L., Spaggiari, A., Gatt, R., Farrugia, P.S. and Grima, J.N. (2023), "Design of isotropic 2D chiral metamaterials based on monohedral pentagonal tessellations", *Thin-Walled Structures*, Vol. 187, p. 110739, doi: 10.1016/j.tws.2023.110739.

Mizzi, L., Attard, D., Gatt, R., Pozniak, A.A., Wojciechowski, K.W. and Grima, J.N. (2015), "Influence of translational disorder on the mechanical properties of hexachiral honeycomb systems", *Composites Part B: Engineering*, Vol. 80, pp. 84-91, doi: 10.1016/j.compositesb.2015.04.057.

Mizzi, L., Attard, D., Gatt, R., Dudek, K.K., Ellul, B. and Grima, J.N. (2021), "Implementation of periodic boundary conditions for loading of mechanical metamaterials and other complex geometric microstructures using finite element analysis", *Engineering with Computers*, Vol. 37 No. 3, pp. 1765-1779, doi: 10.1007/s00366-019-00910-1.

Mizzi, L., Azzopardi, K.M., Attard, D., Grima, J.N. and Gatt, R. (2015), "Auxetic metamaterials exhibiting giant negative poisson's ratios", *Physica Status Solidi (RRL) – Rapid Research Letters*, Vol. 9 No. 7, pp. 425-430, doi: 10.1002/pssr.2015101.78.

Mizzi, L. and Spaggiari, A. (2020), "Lightweight mechanical metamaterials designed using hierarchical truss elements", *Smart Materials and Structures*, Vol. 29 No. 10, p. 105036.

Mizzi, L. and Spaggiari, A. (2021), "Chiralisation of euclidean polygonal tessellations for the design of new auxetic metamaterials", *Mechanics of Materials*, Vol. 153, p. 103698, doi: 10.1016/j.mechmat.2020.103698.

Mizzi, L. and Spaggiari, A. (2022), "Novel chiral honeycombs based on octahedral and dodecahedral Euclidean polygonal tessellations", *International Journal of Solids and Structures. Elsevier Ltd*, Vol. 238, p. 111428, doi: 10.1016/j.ijsolstr.2022.111428.

Mousanezhad, D., Haghpanah, B., Ghosh, R., Hamouda, A.M., Nayeb-Hashemi, H. and Vaziri, A. (2016), "Elastic properties of chiral, anti-chiral, and hierarchical honeycombs: a simple energy-based approach", *Theoretical and Applied Mechanics Letters*, Vol. 6 No. 2, pp. 81-96.

Papadopoulou, A., Laucks, J. and Tibbits, S. (2017), "Auxetic materials in design and architecture", *Nature Reviews Materials*, Vol. 2 No. 12, p. 17078.

Park, Y.J. and Kim, J.K. (2013), "The effect of negative Poisson's ratio polyurethane scaffolds for articular cartilage tissue engineering applications", *Advances in Materials Science and Engineering*, Vol. 2013, doi: 10.1155/2013/853289.

Prall, D. and Lakes, R.S. (1997), "Properties of a chiral honeycomb with a Poisson's ratio of −1", *International Journal of Mechanical Sciences*, Vol. 39 No. 3, pp. 305-314.

Ren, X., Das, R., Tran, P., Ngo, T.D. and Xie, Y.M. (2018), "Auxetic metamaterials and structures: a review", *Smart Materials and Structures*, Vol. 27 No. 2, p. 23001.

Scarpa, F., Giacomin, J.A., Bezazi, A. and Bullough, W.A. (2006), "Dynamic behavior and damping capacity of auxetic foam pads", *Smart Materials and Structures*, p. 61690T. doi: 10.1117/12.658453.

Schenk, M. and Guest, S.D. (2013), "Geometry of miura-folded metamaterials", *Proceedings of the National Academy of Sciences*, Vol. 110 No. 9, pp. 3276-3281, doi: 10.1073/pnas.1217998110.

Shim, J., Shan, S., Kosmrlj, A., Kang, S.H., Chen, E.R., Weaver, J.C. and Bertoldi, K. (2013), "Harnessing instabilities for design of soft reconfigurable auxetic/chiral materials", *Soft Matter*, Vol. 9 No. 34, pp. 8198-8202, doi: 10.1039/c3sm51148k.

Shiyin, X., Xiuchang, H. and Hongxing, H. (2015), "A study on the isolation performance of trichiral lattices with gradient geometry', JVC", */Journal of Vibration and Control*, Vol. 21 No. 16, pp. 3465-3475, doi: 10.1177/1077546314524261.

Sigmund, O., Torquato, S. and Aksay, I.A. (1998), "On the design of 1-3 piezocomposites using topology optimization", *Journal of Materials Research*, Vol. 13 No. 4, pp. 1038-1048, doi: 10.1080/08905459708945415.

Silverberg, J.L., Evans, A.A., Mcleod, L., Hayward, R.C., Hull, T., Santangelo, C.D. and Cohen, I. (2014), "Using origami design principles to fold reprogrammable mechanical metamaterials", *Science*, Vol. 345 No. 6197, pp. 647-650, doi: 10.1126/science.1252876.

Spadoni, A., Ruzzene, M., Gonella, S. and Scarpa, F. (2009), "Phononic properties of hexagonal chiral lattices", *Wave Motion*, Vol. 46 No. 7, pp. 435-450, doi: 10.1016/j.wavemoti.2009.04.002.

Spadoni, A. and Ruzzene, M. (2007), "Numerical and experimental analysis of the static compliance of chiral truss-core airfoils", *Journal of Mechanics of Materials and Structures*, Vol. 2 No. 5, pp. 965-981.

Stratasys (2017), "ABSplus-P430 production-grade thermoplastic for 3D printers", available at: https://support.stratasys.com/en/materials/fdm/absplus-p430 (accessed 20 April 2023).

Strek, T., Jopek, H. and Nienartowicz, M. (2015), "Dynamic response of sandwich panels with auxetic cores", *Physica Status Solidi (b)*, Vol. 252 No. 7, pp. 1540-1550, doi: 10.1002/pssb.201552024.

Suquet, P.M. (1987), *Homogenization Techniques for Composite Media*, Springer-Verlag, Berlin.

Valente, J., Plum, E., Youngs, I.J. and Zheludev, N.I. (2016), "Nano- and micro-auxetic plasmonic materials", *Advanced Materials*, Vol. 28 No. 26, pp. 5176-5180, doi: 10.1002/adma.201600088.

Wan, H., Ohtaki, H., Kotosaka, S. and Hu, G. (2004), "A study of negative Poisson's ratios in auxetic honeycombs based on a large deflection model", *European Journal of Mechanics – A/Solids*, Vol. 23 No. 1, pp. 95-106, doi: 10.1016/j.euromechsol.2003.10.006.

Wang, Z. and Hu, H. (2014), "Auxetic materials and their potential applications in textiles", *Textile Research Journal*, Vol. 84 No. 15, doi: 10.1177/00405175124490.

Wang, X., Qin, R. and Chen, B. (2021), "Laser-based additively manufactured bio-inspired crashworthy structure: energy absorption and collapse behaviour under static and dynamic loadings", *Materials & Design*, Vol. 211, p. 110128.

Wojciechowski, K.W. (1989), "Two-dimensional isotropic system with a negative poisson ratio", *Physics Letters A*, Vol. 137 Nos 1/2, pp. 60-64, doi: 10.1016/0375-9601(89)90971-7.

Wu, W., Hu, W., Qian, G., Liao, H., Xu, X. and Berto, F. (2019), "Mechanical design and multifunctional applications of chiral mechanical metamaterials: a review", *Materials & Design*, Vol. 180, p. 107950.

Zhang, X., An, C.C., Shen, Z.F., Wu, H.X., Yang, W.G. and Bai, J.P. (2020), "Dynamic crushing responses of bio-inspired re-entrant auxetic honeycombs under in-plane impact loading", *Materials Today Communications*, Vol. 23, p. 100198.

Zhang, J. and Lu, G. (2023), "Energy absorption of re-entrant honeycombs in tension and compression", *Engineering Structures*, Vol. 288, p. 116237.

Zheludev, N.I. and Plum, E. (2016), "Reconfigurable nanomechanical photonic metamaterials", *Nature Nanotechnology*, Vol. 11 No. 1, pp. 16-22, doi: 10.1038/nnano.2015.302.

Zhong, R., Minghui, F., Qiuyun, Y., Outeng, X. and Lingling, H. (2019), "Special characteristics of tetrachiral honeycombs under large deformation", *International Journal of Solids and Structures*, Vol. 169, pp. 166-176, doi: 10.1016/j.ijsolstr.2019.04.020.

Zhu, Y., Zeng, Z., Wang, Z.P., Poh, L.H. and Shao, Y.B. (2019), "Hierarchical hexachiral auxetics for large elasto-plastic deformation", *Materials Research Express*, Vol. 6 No. 8, p. 85701.

Zied, K., Osman, M. and Elmahdy, T. (2015), "Enhancement of the in-plane stiffness of the hexagonal re-entrant auxetic honeycomb cores", *Physica Status Solidi (b)*, Vol. 252 No. 12, pp. 1-8, doi: 10.1002/pssb.201552164.

Corresponding author

Luke Mizzi can be contacted at: luke.mizzi@unimore.it